Available online at www.sciencedirect.com
ScienceDirect
Journal of Geodynamics 42 (2006) 63–84
JOURNAL OF GEODYNAMICS
http://www.elsevier.com/locate/jog

Understanding of the geological and geodynamic controls on the formation of the South China Sea: A numerical modelling approach

Bin Xia [a,*], Y. Zhang [b], X.J. Cui [a], B.M. Liu [a], J.H. Xie [a], S.L. Zhang [a], G. Lin [a]

[a] *Key Laboratory of Marginal Sea Geology, Guangzhou Institute of Geochemistry, Chinese Academy of Sciences, Guangzhou 510640, China*
[b] *CSIRO Exploration & Mining, P.O. Box 1130, Bentley, WA 6102, Australia*

Received 19 October 2005; received in revised form 5 May 2006; accepted 8 June 2006

Abstract

A number of previous models have been proposed to explain the formation of the South China Sea, the largest marginal sea basin in Southeast Asia, but no consensus has been reached. In this work, two-dimensional (2D) plan-view models (linear viscous rheology) are constructed to simulate the India–Eurasia collision, its resultant intra-plate deformation and lateral motion along the Red River Fault. We then use 2D cross-section models (a combination of linear viscous rheology and elastic–plastic rheology) to simulate the influence of deep asthenosphere upwelling on lithospheric deformation.

The plan-view models show that the India–Eurasia collision can result in extensive east-southeastward tectonic extrusion, consistent with the prediction of the analogue experiments. During extrusion, the modelled Red River Fault first experienced huge left-lateral shearing and then changed to right-lateral shearing (reversal). The style of shearing motion along the Red River Fault is a function of the distance between the fault and the India–Eurasia collision frontier, which decreases with time and controls relative extrusion movement between the South China Block and Indochina Block. Our models also show that the extrusion can generate extension in an approximately N-S direction in the region containing the present-day South China Sea. Our cross-section models further demonstrate that such horizontal extension can only generate limited thinning of the continental lithosphere in the South China Sea region. In contrast, asthenosphere upwelling is much more efficient in generating lithospheric upper mantle thinning but still inefficient for crust thinning. It is the combination of mechanical extension and asthenosphere upwelling that proves to be the most efficient way to thin the entire lithosphere, and that represents the most likely driving mechanism for the opening and spreading of the South China Sea.

Keywords: South China Sea; Red River Fault; India–Eurasia collision; Numerical modelling

1. Introduction

The South China Sea (SCS) is one of several major marginal sea basins in Southeast Asia. It is located tectonically at the junctions of the Indo-Australia plate, Eurasian plate and Pacific plate (Fig. 1). This suggests that the opening

* Corresponding author. Fax: +86 20 8529 0032.
E-mail address: xiabin@gig.ac.cn (B. Xia).

0264-3707/$ – see front matter © 2006 Elsevier Ltd. All rights reserved.
doi:10.1016/j.jog.2006.06.001

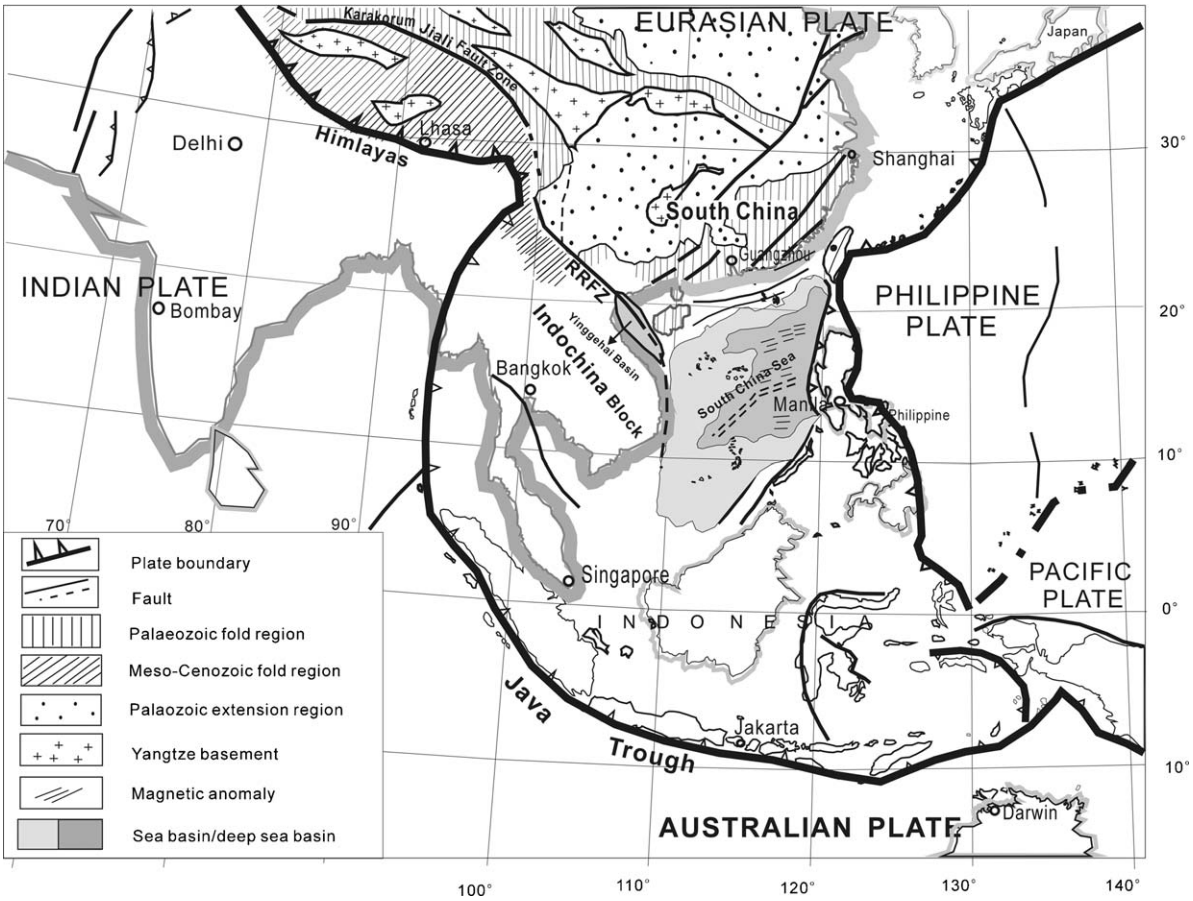

Fig. 1. Schematic map of tectonic and structural outline of the Southeast Asia and neighbouring regions. In the South China Sea area, the plan-view geometry of the oceanic crust is highlighted by the darker grey region within thin lines and magnetic anomaly lineation is illustrated by dashes.

and tectonic evolution of the SCS in the Cenozoic were genetically linked to the complex geodynamic processes associated with the interactions between all the three plates. For this reason, the SCS has attracted intensive structural and geophysical research over the past decades, with a focus on its opening/extensional history and relevant dynamic-tectonic models (e.g. Taylor and Hayes, 1980, 1983; Taylor and Rangin, 1988; Tapponnier and Molnar, 1976; Tapponnier et al., 1982, 1986; Lee and Lawver, 1995; Zhou et al., 1995). There has also been extensive research effort focusing on the stratigraphic structure of the sedimentary sequences of the SCS (e.g. Holloway, 1982; Kudrass et al., 1986; Wu, 1988; Lin et al., 2003), where excellent natural resource potential (e.g. hydrocarbon) exists.

There are numerous tectonic scenario models for the formation of the SCS. These models can be divided into three major groups of hypotheses. The first hypothesis attributes the formation of the SCS to the India–Eurasia continental collision and the collision-resultant tectonic extrusion process (Tapponnier and Molnar, 1976; Tapponnier et al., 1982, 1986). These authors used the similarity between the present-day structural framework in the Southeast Asia and the geometrical features derived from their analogue experiments, and proposed a series of chain-reaction processes leading to the formation of the SCS. The processes include: (1) the India–Eurasia collision led to propagating tectonic extrusion eastward, away from the collision zone; (2) the extrusion led to huge left-lateral shearing along the Red River Fault; (3) finally the shearing and free-rotation along the Red River Fault led to the opening of the SCS as a pull-apart basin. This scenario is supported by evidence from fault movements in the region (e.g. the Ailao Shan-Red River shear zone) and certain magnetic anomaly features in the SCS (e.g. Tapponnier et al., 1990; Briais et al., 1993; Leloup et al., 1995; Lacassin et al., 1997). However, the collision-extrusion model has been challenged by the results of several studies. Houseman and England (1986) and England and Houseman (1986) numerically simulated strain distribution associated with the India-Asia collision zone, and suggested that collision-resultant kinematic energy

was predominantly absorbed by intra-plate shortening deformation and lateral faulting movements, which post-dated crustal thickening, only occurred at smaller scale. England and Molnar (1990) and McKenzie (1990) proposed that there existed widespread right-lateral rotation in the areas east of Tibet and eastward extruding materials were dominantly accommodated by E-W-directed shortening with little impact on Southeast Asia. Shen et al. (2000) argued that the SE-directed extrusion in the Red River-Northwest SCS region only represents approximately 25% of the total extruding material from Himalayas and thus it could not possibly lead to the 700 km extension in the SCS. Davy and Cobbold (1988) also highlighted crustal thickening in the Tibetan Plateau and surrounding areas, based on the results of their indentation analogue experiments.

The second hypothesis emphasizes the drive of the extensional force from an upwelling mantle plume on the formation of the SCS. A number of authors suggested the presence of an anomalous, Dupal-type mantle domain beneath the regions surrounding the SCS in the Cenozoic, based on the petrological and geochemical characteristics of the Cenozoic basalt and mantle xenolith from the Southeast seaboard of China (e.g. Zhu and Wang, 1989; Xie et al., 1989; Fan and Menzies, 1992). The results of a geochemical study of the basalt directly from the SCS sea floor also pointed to the presence of a mantle plume there in the Cenozoic (Tu and Xie, 1992). It has been further inferred that the formation of the SCS and associated sub-basins is related the presence of mantle plume and sideways mantle flow (e.g. Wang et al., 1995; Gong and Li, 1997; Li et al., 1998; Zhu et al., 2002), after the closure of the Tethyan ocean associated with the India- Eurasia collision. Although the precise way in which mantle plume and flow affected the opening the SCS is yet to be explored, the geological signatures (geochemistry, in particular) of such mantle processes seem to be quite obvious.

The third hypothesis (Hawkins et al., 1990; Stern et al., 1990; Aubouin, 1990; Lan et al., 1996) relates the formation of the SCS to the subduction processes of the Pacific plate along the south-eastern margin of the Eurasia plate. This is partially based on the fact that numerous marginal sea basins are located near the western margin of the Pacific plate. According to this model, the SCS is essentially a back-arc basin as a result of subduction-related back-arc extension. However, Zhu et al. (2002) reported that the geochemical characteristics of volcanic rocks formed during the opening of the SCS display strong affinity to the Indian Ocean mantle domain but no affinity to the Pacific subduction zone. They argued it is unlikely that the opening of the SCS is related to the subduction of the western Pacific plate and the associated back-arc extension.

Thus, while there has been extensive research on the SCS and a rather comprehensive understanding of the possible mechanisms for the opening of the SCS, there is still lack of consensus about how the SCS was formed exactly (see Xia et al., 2004). For example, the questions still remain as to: (1) Can the India–Eurasia collision generate sufficient east-southeastward extrusion and lateral shearing along the Red River Fault, which could led to the opening of the SCS? (2) Can the India–Eurasia collision and associated tectonic extrusion lead to broad horizontal extension in the region of the Southeast Asia? (3) How does the presence of mantle plume or the process of mantle upwelling affect crustal/lithospheric deformation under the setting of the India–Eurasia collision? This paper sets out to explore these questions by presenting the results of conceptual numerical models.

2. Tectonic setting

The SCS is a Cenozoic, approximately SW-NE trending, wedge-shaped oceanic basin with an area of about 3,000,000 km^2 (Fig. 1). In the north, it fringes the South China mainland with a passive continental margin and broad shelf areas; the long axis of the SCS oceanic crust is parallel to the South China coastline. In the west, the basin adjoins the Indochina Block also with a passive continental margin, but the shelf area here is much narrower. To the south, the basin is separated from an extinct subduction zone along the Sunda Shelf, Borneo and Palawan by Reed Bank and other shelf areas (Taylor and Hayes, 1980). The eastern margin of the SCS is bounded by an approximately N-S trending active subduction zone along the Manila Trench west of the Luzon arc island, which is part of the Western Pacific subduction system.

The Red River (RR) Fault represents a critical link between the SCS and the collision zone (Fig. 1). This NW-SE trending fault is a major crustal discontinuity developed during the India–Eurasia collision and separating South China from Indochina. Movement along the RR Fault is dominated by significant left-lateral shearing over the bulk of the faulting history (e.g. Wu et al., 1989). The exact left-lateral displacement of the fault is difficult to estimate because of lack of continuity of marker-features. It can be anywhere from 200 to 800 km (e.g. Zhong et al., 1989; Ren and Jin, 1996; Rangin et al., 1995; Sun et al., 2003). The extensive work of Leloup et al. (1995) reported that the lowermost

bound of left-lateral offset is greater than 400 km. Such displacement seems to decrease towards the SE end of the fault, where the fault bends towards the SSE direction and the continuity of the fault also becomes poor. The RR fault exhibits right-lateral shearing at the later stage of its history to present-day (Leloup et al., 1995). Note that the RR Fault terminates near the narrower SW end of the wedged-shaped SCS (Fig. 1).

In order to understand the tectonic factors controlling the opening of the SCS, it is necessary to summarize the time sequences of the major tectonic events involved in the formation of the SCS. Based on the information from the reconstruction of Southeast Asia plate tectonics by Lee and Lawver (1995), the "soft" collision between the India and Eurasia plates occurred approximately from 60 to 44 Ma, during which the convergence rate was about 11 cm/year. This was followed by the "hard" collision between the two plates from approximately 44 Ma to present. During the "hard" collision period, the convergence rate was about 6 cm/year at the beginning and gradually dropped to about 4.5–5 cm/year. The full suturing of the two continents likely occurred soon after the beginning of the "hard" collision at ca. 44 Ma. It was after this stage that significant crustal thickening in Tibet and tectonic extrusion towards the east in South China commenced. Liu et al. (2004) dated a series of volcanic rocks in Tibet and reported the ages of syn-collisional, uplift-related volcanism in the range of 32–12 Ma. Several possible time spans, which are reported for major left-lateral shearing along the RR fault (e.g. 35–28 Ma, Schärer et al., 1994; 31–22 Ma, Zhang and Zhong, 1996; 32–15.5 Ma, Briais et al., 1993; 44–20.5 Ma, Lee and Lawver, 1995), are confined within the "hard" collision period. An age of 34 Ma has also been reported for syn-faulting granite porphyry intrusion (Liu et al., 2003).

To the east of the SCS, the evolution of the West Pacific-Philippine Sea and subduction system is closely related to our context. Although there is a suggestion that the Philippine Sea is a trapped sea basin isolated from the Pacific plate when the Pacific Plate changed the direction of motion from NW to WNW at ca. 43 Ma (e.g. Engebretson et al., 1984, 1985), a back-arc basin origin for the Philippine Sea is a more likely scenario based on the presence of volcanic arcs and accretionary wedges (Hayes and Lewis, 1984). Ocean drilling and paleomagnetic data also suggested a clockwise rotation of the Philippine Plate (Jerrard and Sasajima, 1980; Fuller et al., 1991; Koyama et al., 1992). A probable time sequence here is: (1) the Pacific Plate subducted toward the Eurasia Plate during ca. 50–42 Ma, the motion of the Pacific Plate changed from NW to WNW, the Manila trench retreated northward and the Philippine Sea basin formed as a result of back-arc spreading (consistent with back-arc basin scenario); (2) the Philippine Sea Plate continued to subduct toward the Eurasia Plate from ca. 42 to 5 Ma.

Information on the opening age and extension direction of the SCS is mainly from the measurement of the marine magnetic anomalies from the ocean floor of the basin, reported by Taylor and Hayes (1980, 1983). They identified the presence of east trending magnetic anomaly lineations in the eastern half of the SCS and suggested an active extension and spreading period of ca. 32–17 Ma from the mid-Oligocene to the Early Miocene, during which the SCS experienced the first and major extension event in its history. The orientation of these magnetic lineations reflects an extension direction of approximately N-S. This stretching direction probably changed to the NW-SE direction at the southwest tip of the SCS (see Fig. 11 in Lee and Lawver, 1995); in the northwest basin, the magenitic anomalies trend NE-SW (see Fig. 5 in Taylor and Hayes, 1980). There was also a report that the stretching direction of the SCS displayed a broad shift from N-S to NW-SE (Pautot et al., 1986). The opening period of the SCS coincides with both the major India–Eurasia collision period and the subduction period of the Pacific-Philippine Plate towards the Eurasia Plate.

3. Numerical method

3.1. Brief model description

In order to understand the processes that may have contributed to the formation of the SCS, we have constructed two types of 2D numerical models using the material properties in Table 1: (1) plan-view models (see Fig. 2) and (2) cross-section models (see Fig. 9).

The plan-view models aim to simulate the India–Eurasia collision process, and in particular, to address the question whether the collision can generate sufficient eastward tectonic extrusion, lateral shearing or any approximately N-S directed extension. In the thin sheet models of Houseman and England (1986) and England and Houseman (1986), a simple rectangular geometry was used to approximate the geometry of the continent and the most boundaries of the model were not allowed to move horizontally except for the indenting portion of the boundaries. As such, the models were set out to explore crustal thickening. In our current plan-view models, the geometry is based on the reconstruction

Table 1
Mechanical properties of the cross-ection models

Geometrical layer	Rheology	Density (ρ, kg m^{-3})	Bulk modulus (K, Pa)	Shear modulus (G, Pa)	Viscosity (η, Pa s)	Cohesion (C, Pa)	Tensile strength (T, Pa)	Friction angle (ϕ, °)
Upper crust	Elastic–plastic	2700	2.67×10^{10}	1.6×10^{10}		1.2×10^{7}	0.6×10^{7}	30
Lower crust	Viscous	2900	4.67×10^{10}	2.8×10^{10}	5×10^{20}			
Lithospheric upper mantle	Viscous	3300	10.61×10^{10}	5.47×10^{10}	1×10^{21}			
Asthenosphere	Viscous	3210	10.83×10^{10}	5.0×10^{10}	1×10^{20}			

of the relevant plate configuration (Fig. 2). Realistic plate convergence rates and plate collision conditions are used to define the boundary conditions of the models, and the models thus set out to simulate horizontal extrusion movements. However, the models are incapable of simulating crustal thickening due to their 2D nature (see more discussions Section 5). For the convenience of easy description and avoiding repetition, the full description of each model and relevant boundary conditions will be given in the numerical result session below.

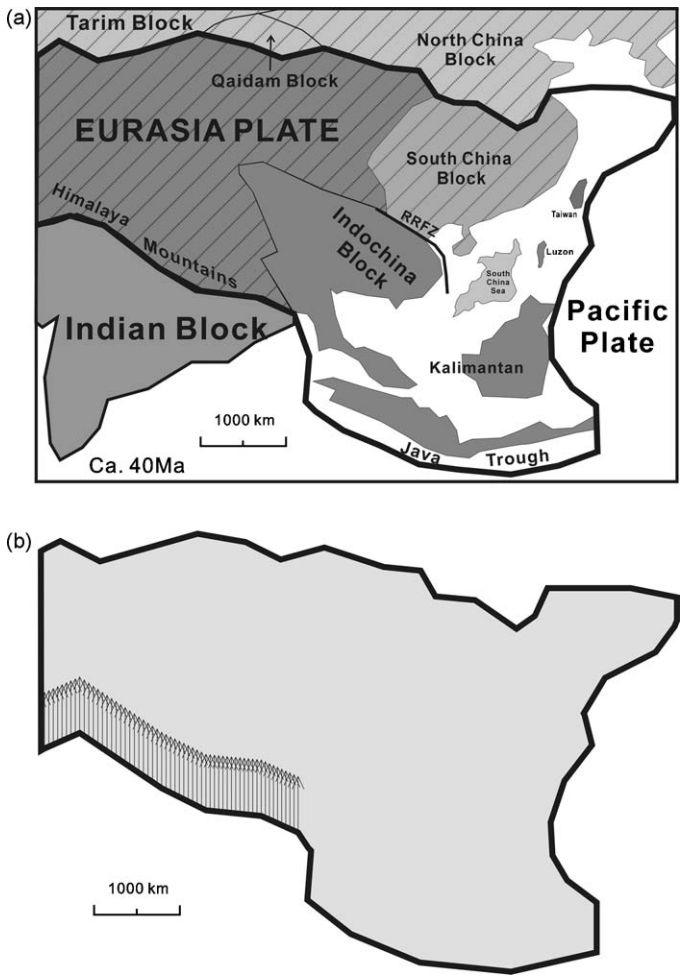

Fig. 2. (a) Geometry of part of the India and Eurasia Plates at ca. 40 Ma, which is involved in the current modelling study (reconstruction and compilation are based on the work of Briais et al., 1993; Rangin et al., 1995; Lee and Lawver, 1995; Taylor and Hayes, 1983). (b) Reconstructed geometry of the Southeast Asia portion of the Eurasia Plate in the plan-view numerical model. Arrows illustrate the convergence rate along the collision segment of the southern boundary of the Eurasia Plate.

After we obtain certain understanding of plate motion-extrusion kinematics from the plan-view models, the cross-section models, approximately parallel to the known extension direction (perpendicular to magnetic anomaly lineation), are then constructed to explore the effects of horizontal extension versus mantle upwelling in leading to lithosphere thinning or break-up (see descriptions in a section below for the details of the models).

3.2. Numerical code

In this study, a finite difference code, Fast Lagrangian Analysis of Continua (FLAC, Cundall and Board, 1988; Itasca, 2000), has been used to simulate rock deformation. Similar to most mesh-based numerical modelling methods, bodies of rocks in FLAC are represented by elements, which form a mesh to fit the geometries of the geological structures to be simulated. Each element is assigned material properties, such as density and elastic moduli and behaves according to prescribed mechanical constitutive laws in response to the applied boundary conditions. The material can yield, deform and flow, and the mesh deforms and moves with the material accordingly. This explicit, Lagrangian, computation scheme, together with the mixed-discretization technique adopted in FLAC, ensure that material failure and large deformation are modelled accurately. The explicit method and dynamic relaxation scheme employed in FLAC determines that there is no need to form the global stiffness matrix during each time-step of computation, which means that large calculations can be carried out with relatively less memory requirements. However, the time-step must be small enough to ensure convergence and numerical stability (Cundall and Board, 1988).

FLAC has previously been successfully applied to the fields of structural geology (e.g. Hobbs et al., 1990; Ord, 1991; Zhang et al., 1996a,b, 2000; Strayer et al., 2001), tectonics (e.g. Wang et al., 2002; Zhang et al., 1996a,b, 1998) and economic geology (e.g. Ord and Oliver, 1997; Sorjonen-Ward et al., 2002; Zhang et al., 2003). For example, Ord (1991) simulated the uniaxial compression deformation of Gosford sandstone, using FLAC, and demonstrated that the stress–strain relationships from the numerical models for several different confining pressures are consistent with those reported from an experimental work (Edmond and Paterson, 1972).

Since FLAC uses a continuum, Lagrangian approach and does not allow remeshing during computation, a model cannot be deformed indefinitely. As deformation in a model progresses, the mesh is displaced along with the material it represents and this leads to geometrical change or distortion of the mesh. Computation must stop when any of the elements within the mesh becomes too strongly deformed as a result of strain localisation. Therefore, the deformation of a FLAC model (e.g. shortening) may not be able to get to the intensity of deformation observed in convergent plate margin or orogenic belts. However, useful prediction can still be made if we focus on the trend and patterns of deformation attributes and their relevance to geological structures.

3.3. Theoretical basis

The mechanical behaviours of the most structural units in the current models are simulated by an elastic–viscous (Maxwell) rheology. This material is equivalent to a combination of an elastic element and a Newtonian viscous element in series (see Ranalli, 1987, p. 82; Turcotte and Schubert, 1982, p. 337), in which the instantaneous elastic response and the viscous deformation are coupled. The total strain (ε_{ij}) is the sum of the elastic strain (ε^{e}_{ij}) and viscous strain (ε^{v}_{ij}),

$$\varepsilon_{ij} = \varepsilon^{e}_{ij} + \varepsilon^{v}_{ij}. \tag{1}$$

The elastic strain relates to stress (σ_{ij}) according to Hooke's law

$$\sigma_{ij} = 2G\varepsilon^{e}_{ij} + \left(K - \frac{2}{3}G\right)\delta_{ij}\varepsilon^{e}_{kk}, \tag{2}$$

where G, K and δ_{ij} are shear and bulk moduli and the Kronecker delta, respectively, and the viscous strain rate ($\dot{\varepsilon}^{v}_{ij}$) relates linearly to stress according to the Newtonian flow law

$$\sigma_{ij} = 2\eta\dot{\varepsilon}^{v}_{ij} - \frac{2}{3}\eta\delta_{ij}\dot{\varepsilon}^{v}_{kk}, \tag{3}$$

where η is viscosity. Strain rate is defined as a function of velocity gradients.

In general, the linear rheology above describes the behaviour of materials, which show instantaneous elasticity but flow viscously under small stresses and over a long period. This rheology can predict the irrecoverable deformation of rocks at high temperatures, slow strain rates and high confining pressures. In the current simulations, we have adopted low and geologically realistic strain rate, and a carefully selected set of material properties including shear and bulk moduli, and viscosity (see more description below). By so doing, we ensure elastic strain component (ε_{ij}^{e}) is negligible and the viscous strain component (ε_{ij}^{v}) becomes predominant. In other words, the rheological behaviour of the current model can essentially be described by a Newtonian viscous law as given in Eq. (3). Adoption of the linear viscous constitutive law above is mainly for simplicity. Similar approach can be found in a number of previous numerical simulation studies in the fields of structural geology and tectonics (e.g. Dieterich and Carter, 1969; Treagus, 1973; Williams et al., 1978; Lin et al., 2004). Our future models may consider more complex temperature dependent, non-linear power creep law.

The cross-section models also involve the use of the Mohr–Coulomb elastic–plastic constitutive law (e.g. Vermeer and de Borst, 1984). A Mohr–Coulomb elastic–plastic material undergoing deformation behaves initially elastically until the stress reaches a critical value known as the yield stress, at which point it begins to deform plastically, and irreversibly, to high strain. The yield of such material may be expressed as a yield function, f, given by

$$f = \tau_{\mathrm{m}} + \sigma_{\mathrm{m}} \sin\phi - C\cos\phi, \tag{4}$$

where τ_{m} is the maximum shear stress, σ_{m} the mean stress, ϕ the friction angle and C is the cohesion. The material is in an elastic state if $f<0$ (the stress state is not touching the yield surface), and is in a plastic state if $f=0$ (the stress state is touching the yield surface). Detailed information on using the Mohr–Coulomb elastic–plastic materials to simulate deformation in thrust wedge can be found in Strayer et al. (2001).

4. Model and results

4.1. Plan-view models: the India–Eurasia collision

4.1.1. Collision-resultant tectonic extrusion

Our first plan-view model simulates the scenario essentially explored by Tapponnier et al. (1982) using an analogue experiment with unilaterally confined boundary conditions. The model adopts the plate geometry and convergence (collision) rate based on the results of previous plate tectonics reconstruction work. The interest here is in the tectonic transport pattern and stress field of South China and Indochina, resultant from the India–Eurasia collision.

The geometry (Fig. 2a) of the relevant portion of the Eurasia plate at ca. 40 Ma, which was reconstructed by Lee and Lawver (1995), is adopted as the basis for the initial geometry of the current model (Fig. 2b). This stage roughly represents a time in the tectonic history of the region when the India Plate and the Eurasia Plate became sutured, and "hard" collision started (Lee and Lawver, 1995). Therefore, the area simulated using a finite difference mesh in this model includes the regions north of the India–Eurasia collision frontier zone and the Java Trough, and south of the Tarim Block, Qaidam Block and the North China Block (see Fig. 2b). The east boundary of the model is speculatively defined to approximate the eastern margin of the western Philippine Sea. A homogeneous material model is adopted here, and the material properties include a density of 2800 kg/m^3, a viscosity of 5×10^{21} Pa s, bulk modulus of 4×10^{10} Pa and a shear modulus of 2.4×10^{10} Pa. These properties are consistent with the parameters for general average crust–lithosphere materials (e.g. Turcotte and Schubert, 1982). The adoption of a homogeneous material model without internal structures is mainly for simplicity. This enables us to explore the first order kinematic effects of collisional plate boundary conditions for the region and to compare with the results of the homogeneous analogue experiments of Tapponnier et al. (1982).

A collision shortening rate of 5.5 cm/year (corresponding to the average convergence rate during the "hard" collision stage, see Lee and Lawver, 1995) is applied to the segment of the south boundary of the model, as illustrated in Fig. 2b. This rate approximately corresponds to an average strain rate range of 0.6×10^{-15} to 0.9×10^{-15} s^{-1}. The combination of such a strain rate and the adopted material properties determines that at least the 99.98% portion of the collision-relevant bulk shortening deformation is accommodated by viscous deformation according to Eqs. (1)–(3) described in a preceding section. The north boundary of the model is fixed, reflecting an "anchor" effect of the Tarim Block, Qaidam Block and North China Block, while the west boundary is not allowed to move in the E-W direction and the east-southeast boundaries are left free. Such boundary conditions are similar to the conditions adopted in the previous

analogue experimental studies (e.g. Tapponnier et al., 1982, 1986). The indenting boundary conditions along the south edge of the model is also similar to that used by Houseman and England (1986) and England and Houseman (1986).

Fig. 3a illustrates the displacement pattern after 12 million years of collision, that is, approximately at 28 Ma; note that at this stage where the maximum displacement reaches 975 km, some elements within the mesh become too strongly deformed and modelling cannot be continued. As clearly shown by the orientations and distributions of displacement vectors, tectonic transport patterns (material movement) are characterized by strong tectonic extrusion toward the east, consistent with the pattern derived from analogue experimental studies (e.g. Tapponnier et al., 1982, 1986). More specifically, materials immediately near the collision frontier move essentially towards the north, reflecting the collision indenting effect from the India Plate, but once away from the collision frontier, materials movement sharply changes direction into predominantly eastward motion. This is because the materials have to escape towards the directions of more free boundaries. There is a difference in tectonic extrusion directions between the east and west portions of the model. In the west half of the model, tectonic transport is essentially east-directed extrusion. In contrast, the extrusion directions of the bulk of the east half (South China and Indochina locations, particularly) display a shift towards the southeast direction. We note that the displacement pattern predicted by the model (Fig. 3a) bears considerable similarity to the pattern of present-day surface movement of China as indicated by GPS data (Fig. 4; Zhang et al., 2002). This similarity provides some validation of the numerical results, and also seems to suggest east to southeastward tectonic extrusion is presently active.

The extent of E-SE tectonic extrusion can be more clearly analysed by plotting out the contours of the displacement components in the E-W direction (Fig. 3b); positive values indicate eastward movement distance. High extrusion is mainly confined to a WNW-ESE trending central zone with the area of the maximum extrusion (>900 km) located east of the east end of the collision frontier (then eastward extrusion starts to decrease from here, toward the east boundary). In contrast, the areas immediately near the collision frontier and near the north boundary of the model show very little extrusion. Such a pattern simply reflects the squeezing effect of the collision zone and the most efficient way for materials to escape.

To evaluate whether the tectonic extrusion can lead to approximately N-S extension in the South China location, we plot out the contours of the displacement components in the N-S direction (Fig. 3c); positive values indicate northward movement and negative values indicate southward movement. Predominantly northward tectonic transport (positive contours) in the west portion of the model (particularly near the collision zone) expectedly reflects strong colliding push. But, it is very encouraging to note that southward tectonic transport (negative contours) dominates the bulk of the east half of the model (locally greater than 400 km). Because the areas near the north edge of the east half of the model show very little southward transport or even northward transport (northeast corner), the kinematic situation here is essentially one where the southeast portion move southward with respect to the north boundary. In other words, as the consequence of collision and east-southeast ward tectonic extrusion, the areas of the model corresponding to South China and Indochina (containing the area of the present-day SCS) creep toward the south, generating a broad extensional regime in the region. The extension is approximately in the north-south direction and is therefore favourable for the opening of the SCS; this is consistent with the known dominant stretching direction in the SCS. The traces of the minimum principal stress axes of the model (Fig. 3d) also show that the directions of extension or deviatoric extension approximately align around the north-south direction in the east-southeast portion of the model. More specifically, the directions of extension (σ_3) are around E-W in the Tibetan Plateau area but change, in the eastern part of the model (corresponding to the east-southeast part of South China), from NNW to NS and then to SSW/SW, reflecting extrusion-related southward extension/rotation. This σ_3 orientation variation pattern is generally consistent with that shown in the world stress map database (Reinecker et al., 2004, www.world-stress-map.org), and also with the stress pattern described by Huchon et al. (1994) for Indochina Peninsula and around eastern syntaxis of Himalaya.

The model above has a free east-southeast boundary. Adoption of such a boundary condition is for an easy comparison with the previous analogue experimental studies (e.g. Tapponnier et al., 1982, 1986). This model boundary condition specification, however, may not reflect the true plate tectonic situation for the region, because plates or micro-plates always interact with each other along all boundaries. To explore the effect of a different, non-free boundary condition, we have constructed another model where the only change of the model is the application of a confining stress (5 MPa) along the east-southeast boundaries, as illustrated in Fig. 5. The results of displacement vectors, E-W displacement components, N-S displacement components and the traces of the minimum principal stress axes are presented in Fig. 6a–d, respectively. It is noted that the patterns and values of the results of the current model are very similar to those for the previous free east-southeast boundary model (see Fig. 3a–d). This consistency indicates that applying a

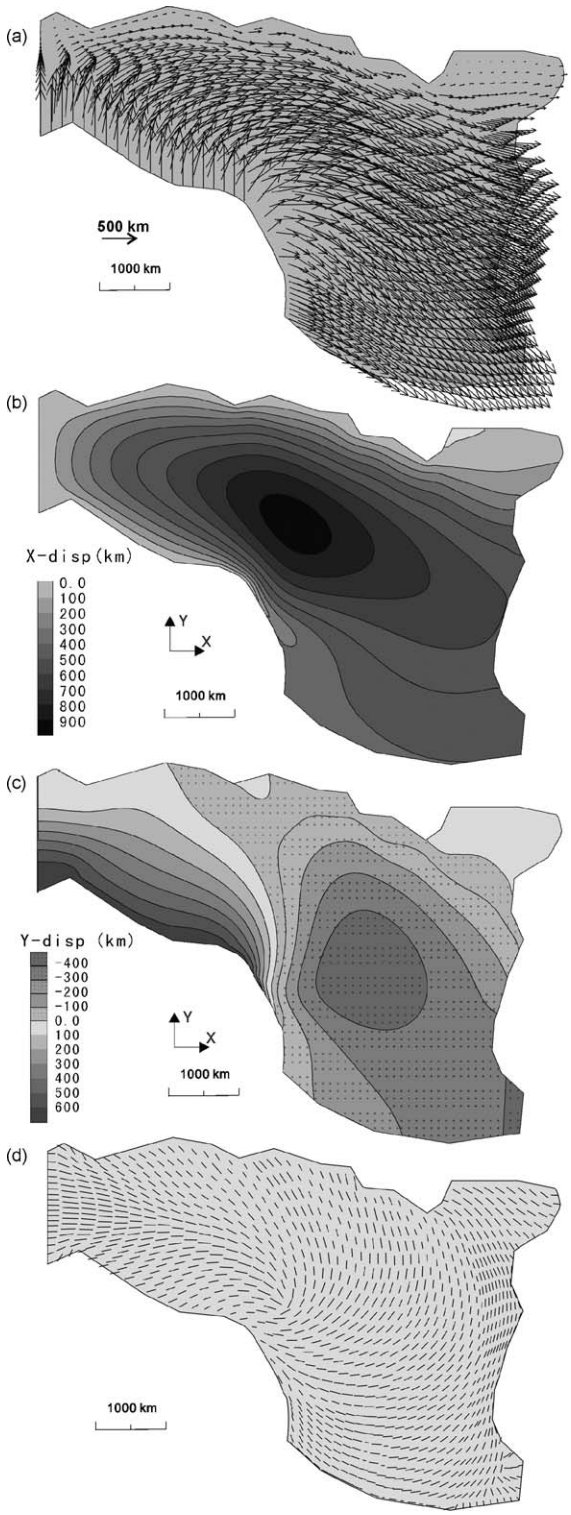

Fig. 3. Results of the plan-view model with free boundary condition along the east and southeast boundaries of the model. (a) Distribution of displacement vectors (the maximum displacement: 975 km). (b) Contours of the *x*-component of displacements. Positive values indicate eastward extrusion. (c) Contours of the *y*-component of displacements. Positive values indicate northward movement and negative values indicate southward movements. (d) Traces of the minimum principal stresses.

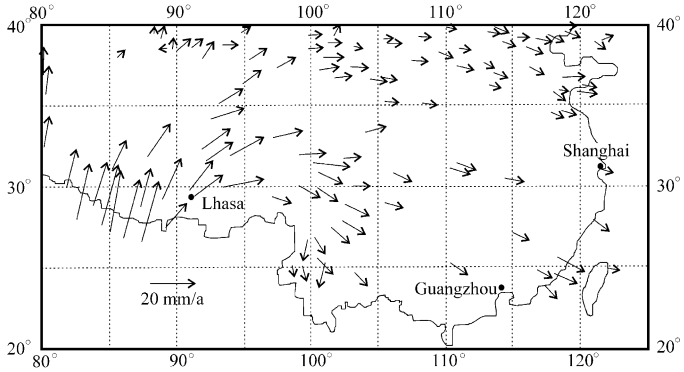

Fig. 4. Surface GPS velocity distribution in China (after Zhang et al., 2002).

small confining stress along the east-southeast boundary, versus a free boundary situation, does not change modelling results. The model results suggest the intensive collision can still lead to east-southeastward tectonic extrusion and generate approximately N-S extension in part of the South China and Indochina region.

4.1.2. Red-River Fault movement during collision

To simulate faulting movement along the RR fault during collision and extrusion, a fault zone is incorporated into the initial geometry of the models (Fig. 7a); geometrical markers are planted on the both side of the fault to track fault offset. The geometry and locations of the RR fault at the early stage of "hard" collision after the India–Eurasia plate suturing is speculated based on several sources of available geological information (e.g. Lee and Lawver, 1994, 1995). The RR fault zone is given a viscosity of 1×10^{20} Pa s, smaller than the surrounding areas, otherwise the rest of material properties and boundary conditions are identical to those used in the first plan-view model above. It needs to be pointed out that there is no direct association between faulting (fault zone strength) and viscosity. In the current model, we assume that the RR fault zone is a weak zone by assigning a lower viscosity to it.

The model is again subject to collisional deformation for about 12 million years. The final geometry and displacement vectors are presented in Fig. 7b. In general, the displacement field is again dominated by the tectonic transport and extrusion toward the east and the southeast, consistent with the patterns displayed by the preceding models. Changes of the positions of the geometrical markers on the both sides of the RR fault highlight the huge left-lateral shearing along the fault. This means that Indochina extruded more towards the southeast than the South China region. The left-lateral offset is maximized at the central segment of the RR fault, reaching about 330 km, and decreases towards the both ends of the fault, showing about 240 km offset near the northwest end and about 180 km near the southeast end. This pattern

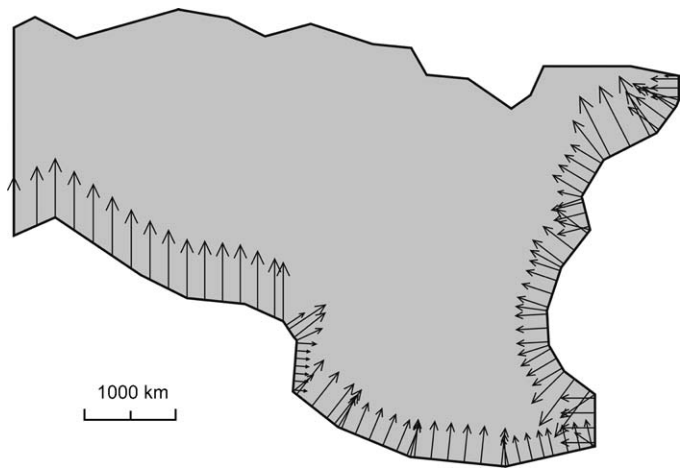

Fig. 5. Geometry and boundary conditions of the plan-view model with supported east and southeast boundaries. North-pointing arrows illustrate India–Eurasia collision related convergence rates, and other arrows indicate the direction of support stresses (see text for more information).

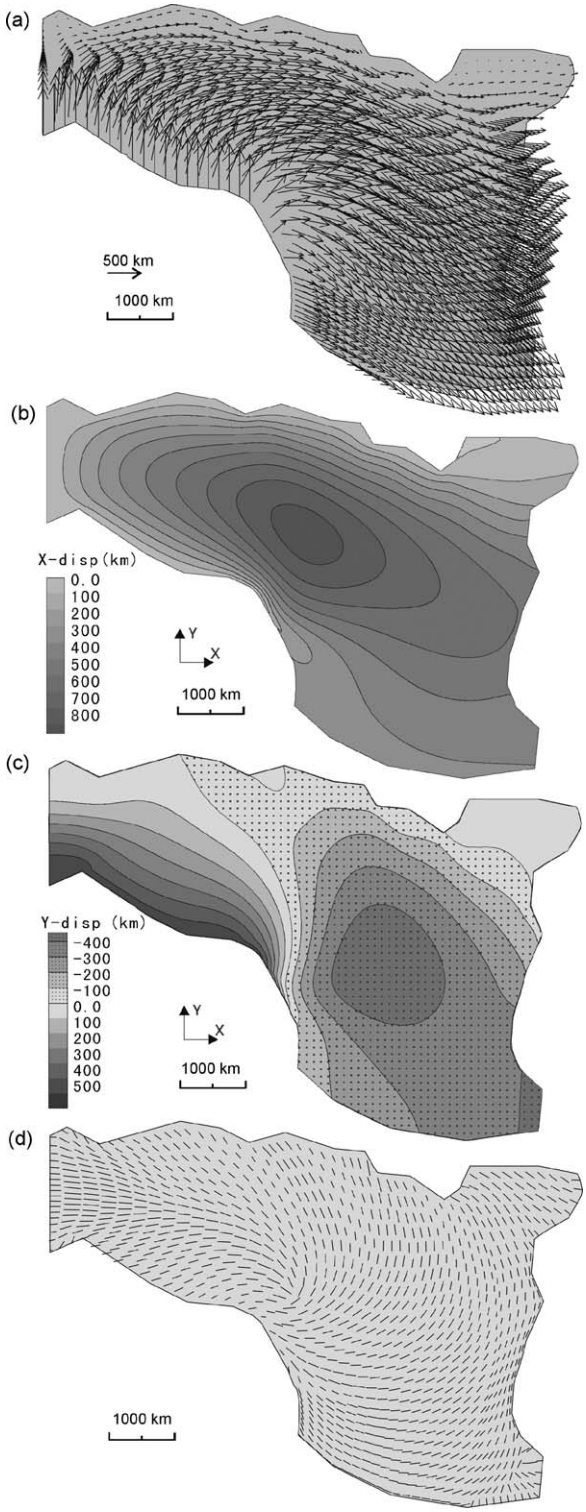

Fig. 6. Results of the plan-view model with stress-support boundary conditions along the east and southeast boundaries of the model. (a) Distribution of displacement vectors (the maximum displacement: 974 km). (b) Contours of the *x*-component of displacements. Positive values indicate eastward extrusion. (c) Contours of the *y*-component of displacements. Positive values indicate northward movement and negative values indicate southward movements. (d) Traces of the minimum principal stresses.

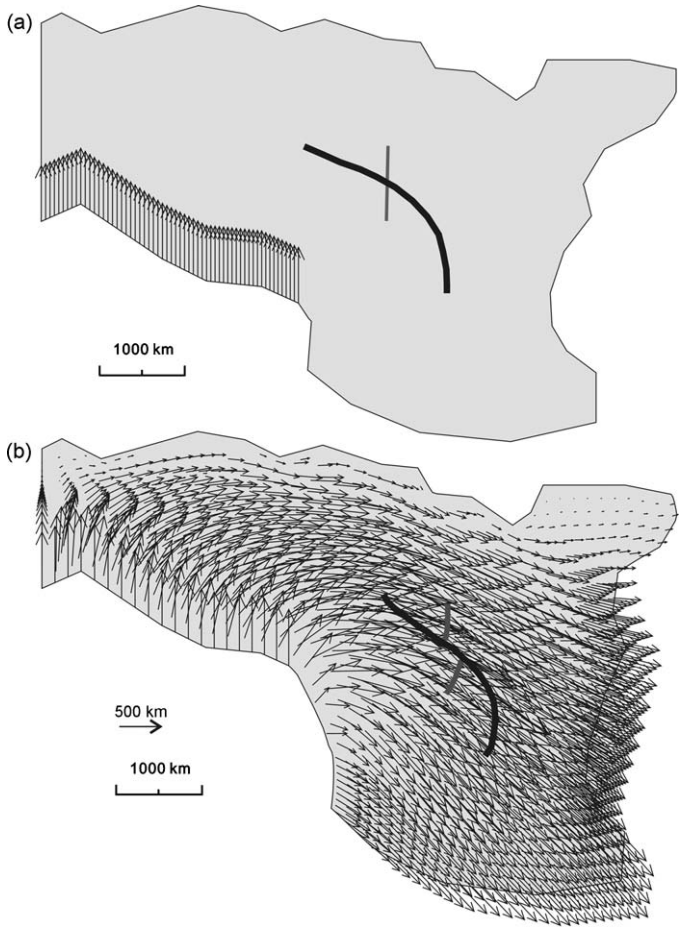

Fig. 7. A plan-view model with the Red River Fault for the early stage of faulting movement. (a) Initial geometry and boundary velocity of model. (b) Displacement vectors and offset along the fault (simulation time corresponds to 12 million year collision and extrusion); the maximum displacement is 1090 km.

of offset distribution is consistent with the general knowledge of fault displacement distribution and is also consistent with the report that left-lateral offset is much smaller toward the southeast end (e.g. Sun et al., 2003; Leloup et al., 1995). However, the left-lateral offsets predicted by the current model is generally smaller than the estimations from previous studies (200–800 km: Zhong et al., 1989; Rangin et al., 1995; Ren and Jin, 1996; Sun et al., 2003; >400 km: Leloup et al., 1995). The potential underestimation of the left-lateral offset along the RR fault in the current model could be due to two reasons: (1) the current model only simulated 12 million years of the collision history, while the left-lateral offset likely took place over a period of more than 20 million years (e.g. 44–20.5 Ma, Lee and Lawver, 1995); (2) the continuum nature of the current model could also underestimate the offset—a model considering discrete sliding along the fault should allow greater offset. It needs to be mentioned that the current model has not included a few other faults in the region, which are smaller than the RR fault but may also be important during the lateral extrusion event.

Simulating faulting movement along the RR fault at a late stage of collision has to be achieved by building a separate model. The continuous simulation of the entire faulting history during collision is not possible using the current continuum approach because the large deformation leads to mesh “collapse” after 12 million year collision. The initial geometry of the late-stage collision and faulting model (Fig. 8a) is speculated with a reference to the present-day geometry (see Fig. 1). The main feature is that the northwest end of the RR fault is close to the collision frontier at the Himalaya. Material properties and boundary conditions are consistent with the preceding models.

The final geometry and displacement vectors of the model after 5 million year further collision are given in Fig. 8b. It is noted that as collision continues, the east-south-eastward tectonic transport and extrusion is still going, as clearly illustrated by displacement vectors. However, faulting along the modelled RR fault shows a reversal in the direction

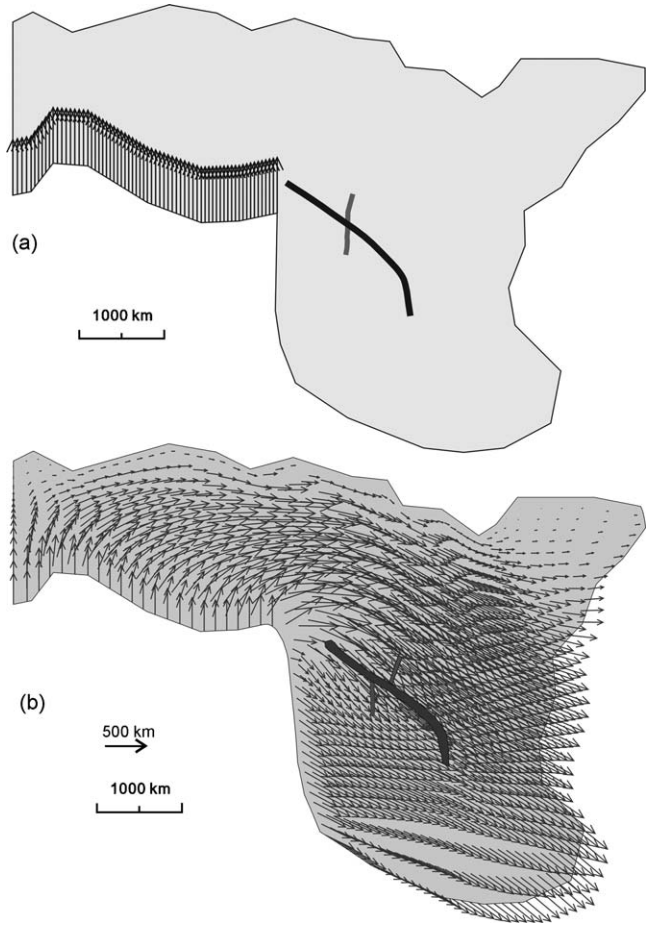

Fig. 8. A plan-view model with the Red River Fault for the late stage of faulting movement. (a) Initial geometry and boundary velocity of model. (b) Displacement vectors and offset along the fault (simulation time corresponds to 6 million year further collision and extrusion); the maximum displacement is 685 km.

of movement, and now right-lateral shearing becomes apparent (see change of positions of geometric markers along the fault in Fig. 8b). The implication of such faulting movement patterns is that the South China region is extruding more than the Indochina region toward the southeast in the late stages of collision. Further discussion on the faulting reversal will be provided in Section 5.

4.2. Cross-section models: effects of horizontal extension versus mantle upwelling

The results of the plan-view collision models point to a scenario where the India–Eurasia collision can lead to significant tectonic extrusion toward the east-southeast, and such tectonic extrusion can result in approximately N-S extension in the South China–Indochina region that contains the present SCS location. However, we still do not have any clue about whether the broad N-S extension is sufficient to lead to the opening of the SCS and how horizontal extension competes with possible deep mantle upwelling in the vertical direction in influencing the opening of the SCS. We now use simple cross-section models to address the questions above. Three tectonic scenarios are explored here: (1) horizontal extension only, (2) asthenosphere upwelling only and (3) horizontal extension plus asthenosphere upwelling.

A conceptual cross section is compiled in a direction parallel to the broad extension direction (roughly N-S) as predicted by the plan-view models above. The section contains four layers, that is, upper crust (elastic–plastic), lower crust (viscous), lithospheric upper mantle (viscous) and asthenosphere (viscous). The initial geometries of the cross sections are shown in Fig. 9 and material properties are given in Table 1. The four layers in the section for scenario-1

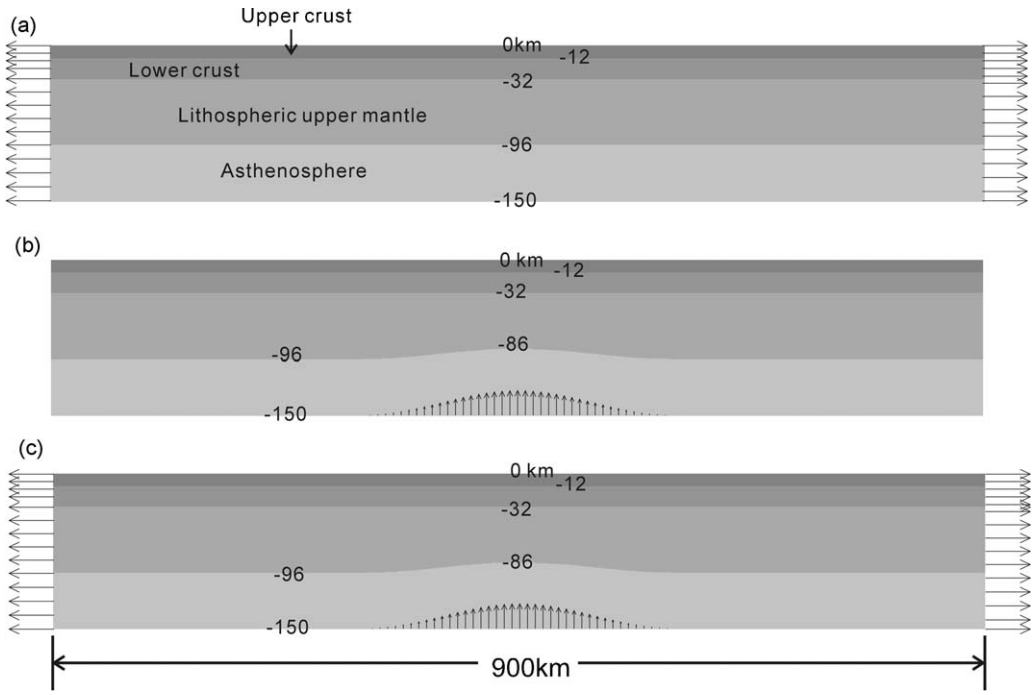

Fig. 9. Geometry and boundary conditions for three cross-section models: (a) Mechanical extension only, (b) asthenosphere upwelling only and (c) combination of mechanical extension and asthenosphere upwelling. The section is 900 km long and 150 km deep.

are all horizontal (Fig. 9a). A stretching displacement rate is applied to the two vertical edges of the model, and the rate is such that a 20% bulk extension is achieved in 6 million years (corresponding to an average strain rate of about 1×10^{-15} s). A similar initial geometry is used in the section for the scenario-2 model (Fig. 9b), but the central segment of the top boundary of the asthenosphere layer is elevated by a small amplitude (10 km), relative to the wavelength, to consider an already-upwelled asthenosphere situation. As illustrated in Fig. 9b, the upwelling rate applied to the base of the asthenosphere layer is varied to approximate the case of an upwelling asthenosphere current. This model is run for 6 million years. The third scenario model (Fig. 9c) adopts an identical geometry as the scenario-2 model, but the horizontal extensional boundary condition of the scenario-1 model and the upwelling asthenosphere boundary condition of the scenario-2 model are all considered in this scenario. Note that the model time of 6 million years is targeted here, simply because this is the model time that can be achieved in all the three models before severely deformed elements emerge within a mesh ("collapse"). The results of these models are presented in Figs. 10–12.

4.2.1. Scenario-1: horizontal extension only

Displacement vectors (Fig. 10a) are predominantly sub-horizontal, reflecting essentially homogeneous horizontal extension. There is lack of any upwelling features in the asthenosphere layer. Crustal and lithospheric thinning is also essentially homogeneous with only minor localisation (Fig. 11a). At the end of 20% bulk extension over the 6 million-year simulation time, the maximum crust and lithosphere thinning is 6.2 km (about 19%) and 17.6 km (about 18%), respectively (Fig. 12). The bulk of the crust/lithosphere slab remains intact. Therefore, horizontal mechanical extension alone has only a limited effect on lithosphere thinning and does not seem to be an efficient mechanism to break a continent for the formation of an oceanic basin.

4.2.2. Scenario-2: asthenosphere upwelling only

In this model, the lateral edges are fixed and thus the bulk horizontal deformation is zero. Any deformation and crust/lithosphere thinning is purely the consequence of asthenosphere upwelling. As is evident from Fig. 10b, the upwelling "current" along the base of the asthenosphere leads to strong upwelling motions of the top boundary of the asthenosphere. This further strongly affects the overlying lithospheric upper mantle and even the base of the lower crust layer, forming a broad upwelling cell. The upwelling material current becomes flatten out sideways towards flanks.

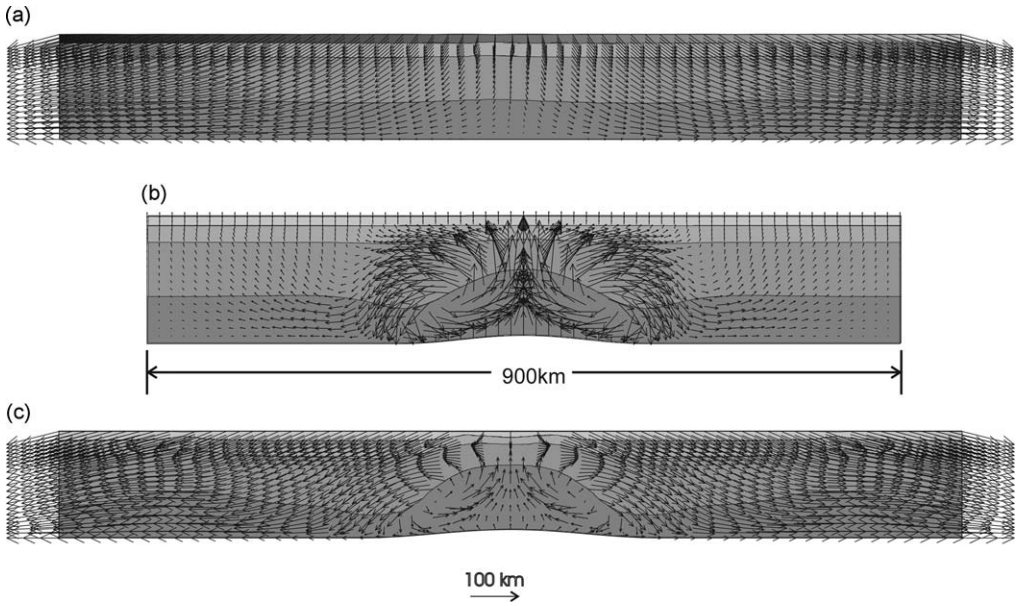

Fig. 10. Distribution of displacement vectors of the cross-section models after a simulation time of 6 million years: (a) mechanical extension only (the maximum displacement: 93.3 km), (b) asthenosphere upwelling only (the maximum displacement: 25.5 km) and (c) combination of mechanical extension and asthenosphere upwelling (the maximum displacement: 92.8 km).

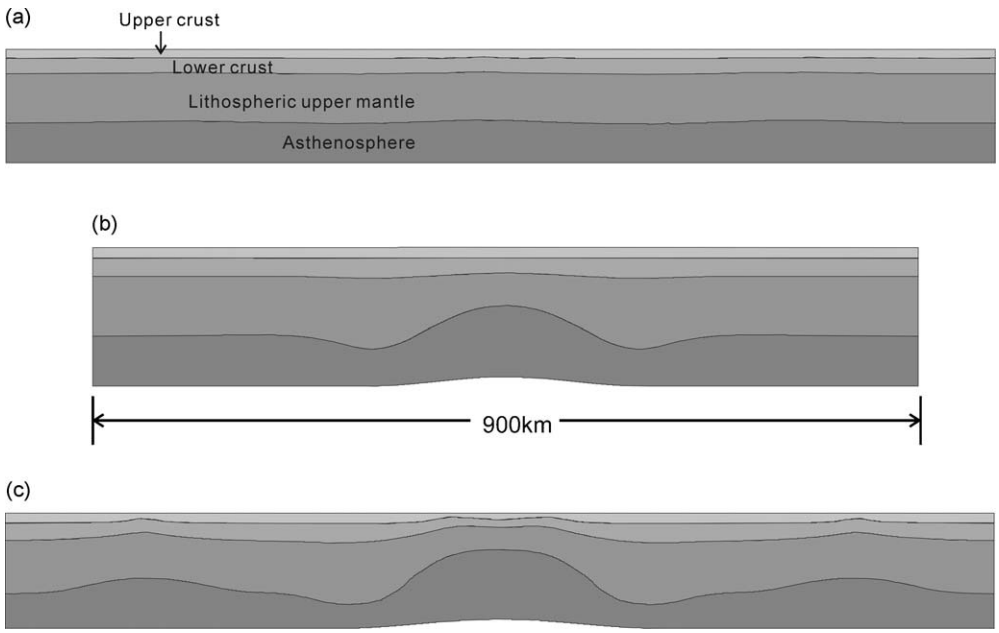

Fig. 11. Final geometries of the cross-section models after a simulation time of 6 million years; note that the changes of layer thickness illustrate the thinning of layers in each model (see Fig. 9 for comparison). (a) Mechanical extension only. (b) Asthenosphere upwelling only. (c) Combination of mechanical extension and asthenosphere upwelling.

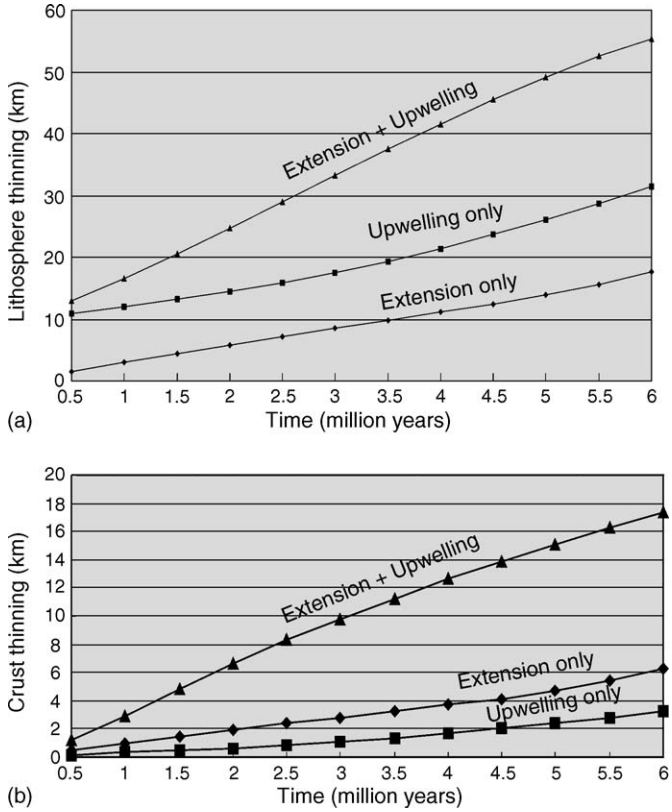

Fig. 12. Plots of variations of thinning with time for three cross-section models: (a) lithosphere thinning and (b) crust thinning.

The upwelling of asthenosphere results in greater local lithosphere thinning (Fig. 11b) than the extension-only case (see Fig. 11a). At the end of the 6 million-year simulation time, the maximum lithosphere thinning is 31.5 km (about 33%; Fig. 12a), much greater than in the extension-only model. However, asthenosphere upwelling appears to have less effect on crust than on lithosphere upper mantle. Fig. 12b shows that the maximum crust thinning of this model is only 3.3 km or about 10%, even less in the extension-only model. Therefore, the thinning here is mainly accommodated by the deformation of lithospheric upper mantle, with only a small portion accommodated by crustal deformation. In summary, asthenosphere upwelling (or mantle plume) seems to have more profound effects on lithosphere thinning than mechanical horizontal extension, and thus represents a more efficient mechanism to break a continent for the formation of an oceanic basin.

4.2.3. Scenario-3: horizontal extension plus asthenosphere upwelling

The displacement field of this model (Fig. 10c) combines features of the extension-only model and the upwelling-only model. Strong subhorizontal material transport dominates the flank areas, while strong upwelling movements prevail in the central segment of the section. Evident subsiding movement is also observed in the crustal domains overlying the asthenosphere upwelling cell. Crust and lithosphere thinning is visually greater than two other scenario models (Fig. 11c; in comparison with Fig. 11a and b). At the end of 20% bulk extension and 6 million-year simulation time, the maximum crust thinning and lithosphere thinning are 17.4 km (about 54.4%) and 55.3 km (about 57.6%), respectively (Fig. 12), much greater than those in the two other models above. Therefore, the combination of tectonic extension and mantle upwelling represents the most efficient mechanism for the thinning of both crust and lithosphere, and also the most efficient way to break a continent for the formation of an oceanic basin.

It needs to be recognized that the crustal and lithosphere thinning of this model still does not reach the extent required for the opening of the SCS; the current mesh-based, continuum approach does not allow further thinning or further deformation of elements (see the model description section). However, the comparison of the results from the three scenario models has provided the prediction of the trend for thinning development.

5. Discussion

5.1. Opening of the South China Sea

As mentioned in Section 1, there are several different hypotheses about the opening of the SCS dominated by the India–Eurasia collision and extrusion theory, the upwelling mantle plume theory and the Pacific Plate subduction theory. It seems that a collision-extrusion genesis for the SCS has been more widely accepted in the geological community (e.g. Tapponnier and Molnar, 1976; Tapponnier et al., 1982, 1986; Lee and Lawver, 1995; Leloup et al., 1995; Zhou et al., 1995). According to this hypothesis, the SCS is a pull-apart basin near the southeast tip of the RR Fault as a result of huge left-lateral shearing along the fault, which is the result of the collision-generated extrusion. This interpretation is supported by the spatial association of the SCS with the RR Fault and the general coincidence between the sea floor spreading time of the SCS and the time for the RR Fault left-lateral motion.

However, the following observations do not seem to be in favour of the pull-apart-basin origin, based on the basic principles of structural geology: (1) the SCS is trending in the NE direction, while the left-lateral shearing along the NW-SE trending RR Fault should generate approximately E-W tensile fracture or wing crack or pull-apart space; (2) the wider opening end of the wedge-shaped SCS is facing away from the RR Fault (see Fig. 1), while the wider opening end of any wing cracks should face and be in contact with the SE tip of the left-lateral shearing RR Fault; (3) the information from the magnetic anomalies of the SCS (e.g. Taylor and Hayes, 1983) seems to suggest that the NE portion of the SCS (E-W extension) opened earlier and experienced greater spreading than the SW tip of the SCS (NW extension), while the situation should be just opposite if the SCS is a pull-apart basin or left-lateral shearing "crack"; (4) the displacement of the RR Fault becomes smaller at the Yinggehai Basin location (200 km, Sun et al., 2003) and it should decrease further toward the SE end of the RR Fault, it is thus questionary whether such displacement alone can generate a pull-apart basin of the SCS size. On the basis of the arguments above, it is unlikely that the SCS is a simple pull-apart basin due to the left-lateral shearing of the RR Fault.

However, the results of the current plan-view numerical models confirm the general kinematics of the collision-extrusion model, that is, the India–Eurasia collision can generate huge east-southeastward tectonic extrusion. In addition, our results also suggest that such extrusion can induce broad, approximately N-S directed extension. But the results of our extension-only cross-section model (see Figs. 10a and 11a) suggest that horizontal mechanical extension alone has only limited effect on crust–lithosphere thinning and probably is not sufficient to lead to the opening of the SCS to the currently observed size.

Mantle upwelling associated with mantle plume is the other possible contributing process, the involvement of which has been evidenced by the petrological and geochemical characteristics of the Cenozoic basalt and mantle xenolith from the SCS and neighbouring regions (e.g. Zhu and Wang, 1989; Xie et al., 1989; Fan and Menzies, 1992; Tu and Xie, 1992; Wang et al., 1995; Gong and Li, 1997; Li et al., 1998; Zhu et al., 2002). Our cross-section model with asthenosphere upwelling (Figs. 10b and 11b) shows that mantle upwelling alone can generate much greater lithosphere thinning than the case of horizontal mechanical extension alone. But thinning via this mechanism is mostly localised in the lithospheric upper mantle layer with minimal thinning in the crustal layers. As such, it would take time for the current of upwelling asthenosphere to eventually break the upper crust layer. Therefore, the combination of horizontal mechanical extension and upwelling asthenosphere represents the most likely scenario for the opening and spreading of the SCS, as demonstrated by the results of the current cross-section model involving the both mechanisms (Figs. 10c and 11c). Joining force from the both mechanisms can lead to more rapid and much greater crust–lithosphere thinning (crust and lithospheric upper mantle are thinned simultaneously) and make it easier to break the continental lithosphere to form the SCS. We would also like to speculate that the configurations of the mantle plume cell and mantle flow currents, together with the approximate N-S direction of collision-resultant, broad horizontal extension, jointly control the trending and geometry of the SCS.

While the horizontal extrusion patterns and stress orientation variations from the current plan-view models are consistent with GPS data (Zhang et al., 2002) and measured stress orientations (Reinecker et al., 2004), crustal thickening has been ignored in these models due to their 2D nature. The models of Houseman and England (1986) and England and Houseman (1986) suggested that convergence between India and Eurasia was primarily accommodated by crustal thickening in front of the indenter. But, the results of these models might be determined by the model boundary conditions where most model edges are not allowed to move laterally (see Fig. 1 in Houseman and England, 1986). Regional crustal thickness data show that there is a sharp change of crustal thickness across the eastern boundary of

the Tibetan Plateau. Crustal thickness is mostly in the range of about 65–75 km in the Plateau, but it drops to about 45–30 km in the broad region of South China (e.g. Xu et al., 2003; Gao et al., 2005). Therefore, it seems that crustal thickening is mainly confined to the Tibetan Plateau, while east-southeastward tectonic extrusion is widespread across the entire region as demonstrated by the pattern of GPS velocities (Fig. 4; also see Zhang et al., 2002), huge strike-slip movements along crustal-scale shear zones (e.g. Leloup et al., 1995) and analogue experiments (Tapponnier et al., 1982). Our current models have predicted such horizontal tectonic transport patterns well. The future effort will be to construct 3D models to examine crustal thickening and its effects on lateral extrusion.

Due to the 2D and continuum nature of our models, the potential influence of subduction along the West Pacific margin has not been explored in this study. This represents a weakness of this work, because back-arc extension associated with the subduction zone or extension in response to any subducting slab roll-back can be one of the important agencies influencing the formation of the SCS. However, we note that the geochemical characteristics of mantle-sourced volcanic rocks in the SCS show strong affinity to the India Ocean mantle domain but no affinity to the Pacific subduction system (Zhu et al., 2002). This suggests the formation of the SCS is probably less related to the Pacific subduction system in comparison with the India–Eurasia collision and deep mantle upwelling process. More geochemical studies are needed to test the geochemical affinity of the SCS and provide more solid evidence.

5.2. *Red River Fault*

The RR fault has been widely recognized as a major lithospheric scale discontinuity in Southeast Asia, which separates the South China Block from the Indochina Block and controls relative movement between the two blocks (e.g. Tapponnier et al., 1990; Leloup et al., 1995; Lee and Lawver, 1995). The most important feature of the fault is that it first experienced huge left-lateral shearing, and then a reversal of lateral motion to right-lateral shearing. The

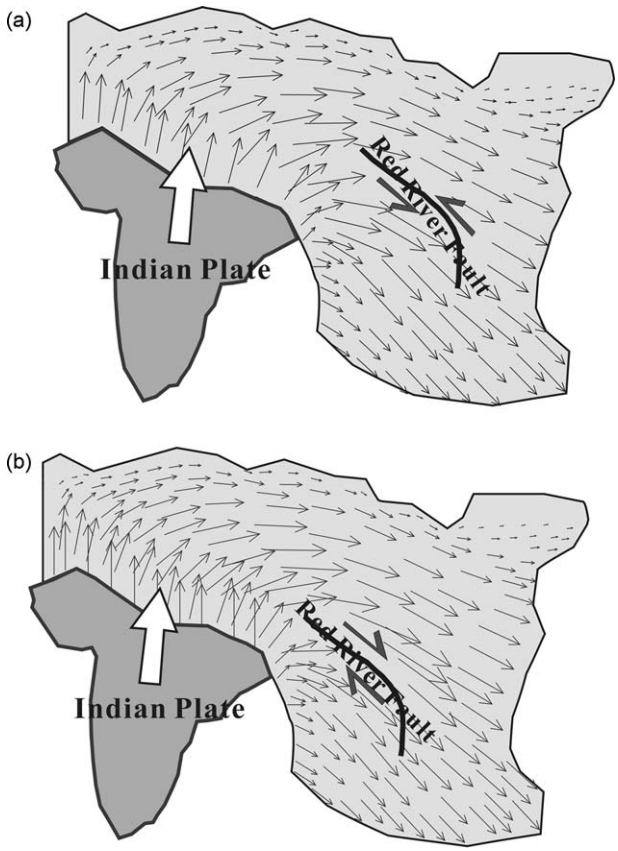

Fig. 13. Cartoons illustrating southeastward extrusion, tectonic movement patterns and sense of shear along the Red River Fault, as a result of India–Eurasia collision: (a) an early stage and (b) a later stage (see text for more explanation).

present-day sense of motion on the fault is right-lateral shearing (e.g. Leloup et al., 1995). The left-lateral shearing probably began at ca. 44 Ma, soon after the onset of "hard" collision (Lee and Lawver, 1995), and possibly lasted to as late as 20 Ma (Wu, 1988) or 17 Ma (Leloup et al., 1995).

The current models could not simulate the entire faulting history along the RR Fault, due to the mesh-related weakness of our continuum approach. However, by selecting two time spans of the faulting history and building two different models, we are able to demonstrate the left-lateral shearing and the right-lateral shearing can occurs at different stages of the India–Eurasia collision and tectonic extrusion. The major difference between our two models is in the distance from the northwest tip of the RR Fault to the collision frontier (see Figs. 7a and 8a). We speculate that the sense of shearing along the RR Fault is a function of this distance between the RR Fault and the India–Eurasia collision frontier.

The primary drive on the regional tectonics is the India–Eurasia collision. This collision resulted in an approximately northward displacement of some 2000 km (see Tapponnier et al., 1982). This huge displacement and associated shortening has to be accommodated by east-southeastward tectonic extrusion (Tapponnier et al., 1982, 1986) and by crustal thickening (England and Houseman, 1986; England and Molnar, 1990; McKenzie, 1990). The tectonic extrusion is the secondary major drive on the tectonics of the region, and it simply means that materials have to escape from the push of India. During this process, the RR Fault was just a weak discontinuity zone allowing differential extrusion across the fault in the most efficient way. As shown by several Southeast Asia reconstruction work (e.g. Lee and Lawver, 1995; Robert, 1997), the RR Fault was far away from the collision frontier and spatially a wide opening existed between the fault and the collision zone. As such, extrusion took place most efficiently through this opening and the Indochina Block extruded faster than the South China Block (Fig. 13a). As a result of this, the motion along the RR Fault was expressed as left-lateral shearing. As collision progressed, the distance between the RR Fault and the collision zone became greatly reduced (as shown by the present-day geometry—see Fig. 1) and the opening was gradually shut. At a certain point (probably around 20–17 Ma), collision-resultant material escape and extrusion would be more efficient through the north side of the RR Fault (Fig. 13b). Therefore, the reversal of motion occurred and the slip along the fault changed to right-lateral shearing. We can speculate that such right-lateral shearing will continue as long as the India–Eurasia continues.

6. Conclusions

The South China Sea situates at the trip junction of the Eurasia Plate, the Indo-Australia plate and Pacific plate, and its formation is the outcome of more than one process. The current plan-view models demonstrate that the India–Eurasia collision can result in extensive east-southeastward tectonic extrusion, consistent with the prediction of previous analogue experimental studies. In the process of such extrusion, the Red River Fault first experienced huge left-lateral shearing and then a reversal of motion changing to the right-lateral shearing. The style of shearing motion along the RR Fault is a function of the distance between the RR Fault and the India–Eurasia collision frontier, which decreases with time and controls relative extrusion movement between the South China Block and Indochina Block.

The models also show that the extrusion gives rise to a broad extension in the approximately N-S direction in the region containing the present-day location of the South China Sea. Our cross-section models demonstrate that such horizontal extension can only generate limited thinning of the continental lithosphere. In contrast, asthenosphere upwelling is a more efficient process to thin the lithosphere, but thinning is mainly localised within the lithospheric upper mantle with crustal layers experiencing very little thinning. It is the combination of mechanical extension and asthenosphere upwelling that proves to be the most efficient mechanism to thin both the crust and lithospheric upper mantle, and represents the most likely drive for the opening and spreading of the SCS. Therefore, a very likely scenario is that the collision-extrusion resultant horizontal extension probably initiated the thinning of the continent lithosphere of then the SCS region, and mantle plume and upwelling derived from complex plate interaction in the region accelerated the thinning and eventually led to the opening and spreading of the SCS.

Acknowledgements

Authors would like to thank two anonymous reviewers for their constructive comments and suggestions, and thank Prof. Giorgio Ranalli for his editorial comments. Financial supports from the Chinese Academy of Sciences (No.

KZCX2-SW-117), the National Natural Science Foundation of China (No. 40534019) and Guangzhou Institute of Geochemistry, CAS (No. GIGCX-04-04) are gratefully acknowledged.

References

Aubouin, J., 1990. Dynamic model of the western Pacific. Tectonophysics 183, 1–7.

Briais, A., Patriat, P., Tapponnier, P., 1993. Updated interpretation of magnetic anomalies and seafloor spreading in the South China Sea: implications for the Tertiary Tectonics of Southeast Asia. J. Geophys. Res. 98 (B4), 6299–6328.

Cundall, P.A., Board, M., 1988. A microcomputer program for modelling large-strain plasticity problems. In: Swoboda, G. (Ed.), Numerical Methods in Geomechanics, vol. 6. Proceedings of the Sixth International Conference on Numerical methods in Geomechanics, pp. 2101–2108.

Davy, P., Cobbold, P.R., 1988. Indentation tectonics in nature and experiments: experiments scaled for gravity. Bull. Geol. Inst. Upsalla 14, 129–141.

Dieterich, J.H., Carter, N.L., 1969. Stress-history of folding. Am. J. Sci. 267, 129–154.

Edmond, J.M., Paterson, M.S., 1972. Volume changes during the deformation of rocks at high pressures. Int. J. Rock Mech. Mining Sci. 9, 161–182.

Engebretson, D.C., Cox, A., Gordon, R.G., 1984. Relative motions between oceanic plates of the Pacific Basin. J. Geophys. Res. 89 (10), 291–310, 310.

Engebretson, D.C., Cox, A., Gordon, R.G., 1985. Relative motions between oceanic and continental plates in the Pacific Basin. Geol. Soc. Am. Spec. Pap. 206, 59.

England, P., Houseman, G., 1986. Finite strain calculations of continental deformation 2: comparison with the India-Asia collision zone. J. Geophys. Res. 91, 3664–3676.

England, P., Molnar, P., 1990. Right-lateral shear and rotation as the explanation for strike-slip faulting in eastern Tibet. Nature 344, 140–142.

Fan, W., Menzies, M.A., 1992. The lithospheric mantle composition of volcanism in extension settings: the geochemical evidence of Cenozoic basalts in Leiqiong area. In: Liu, R. (Ed.), The Ages and Geochemistry of Cenozoic Volcanic Rocks in China. Seismological Publishing House, Beijing, pp. 320–329.

Fuller, M., Haston, R., Lin, J., Richter, B., Schmidtke, E., Almasco, J., 1991. Tertiary paleomagnetism of regions around the South China Sea. J. Southeast Asian Earth Sci. 6 (3–4), 161–184.

Gao, X., Wang, W.M., Tao, Z.X., 2005. Crustal structure of China mainland and its adjacent regions. Chin. J. Geophys. 48 (3), 591–601.

Gong, Z., Li, S., 1997. Analysis of the Continental Marginal Basins and Oil Gas Aggregation of Northern South China Sea. Science Press, Beijing.

Hawkins, J.W., Lonsdale, P.F., Macdougall, J.D., Volpe, A.M., 1990. Petrology of the axial ridge of Mariana Trough backarc spreading center. Earth Planet Sci. Lett. 100, 226–250.

Hayes, D.E., Lewis, S.D., 1984. A geophysical study of the Manila Trench, Luzon, Philippines 1. Crustal structure, gravity, and regional tectonic evolution. J. Geophys. Res. (B) 89 (11), 9171–9195.

Hobbs, B.E., Mühlhaus, H.-B., Ord, A., 1990. Instability, softening and localisation of deformation. In: Knipe, R.J., Rutter, E.H. (Eds.), Deformation Mechanisms, Rheology and Tectonics, vol. 54. Geological Society of London Special Publication, pp. 143–165.

Holloway, N.H., 1982. North Palawan Block, Philippines—its relation to Asian mainland and role in evolution of South China Sea. Am. Assoc. Petrol. Geol. Bull. 66, 1335–1383.

Houseman, G., England, P., 1986. Finite strain calculations of continental deformation 1: method and general results for convergent zones. J. Geophys. Res. 91, 3651–3663.

Huchon, P., Puchon, X.L., Rangin, C., 1994. Indochina peninsula and the collision of India and Eurasia. Geology 22, 27–30.

Itasca, 2000. FLAC: Fast Lagrangian Analysis of Continua, user manual, version 4.0. Itasca Consulting Group, Inc., Minneapolis.

Jerrard, R.D., Sasajima, S., 1980. Paleomagnetic synthesis for southeast Asia: constraints on plate motions. In: Hayes, D.E. (Ed.), The Tectonic and Geologic Evolution of Southeast Asian Seas and Islands. Geophys. Monogr. Ser., vol. 23, pp. 293–316.

Koyama, M., Cisowski, S.M., Pezard, P., 1992. Paleomagnetic evidence for northward drift and clockwise rotation of the Izu-Bonin arc since the early Oligocene. Proc. ODP, Scientific Results 126, 353–370.

Kudrass, H.R., Weidicke, M., Cepek, P., 1986. Mesozoic and cenozoic rocks dregged from the South China Sea (Reed Bank area) and Sulu Sea and their significance for plate tectonic reconstructions. Mar. Petrol. Geol. 3, 19–30.

Lacassin, R., Malushi, H., Leloup, P.H., Tapponnier, P., Hinthong, C., Siribhakdi, K., Chuaviroj, S., Charoenravat, A., 1997. Tertiary diachronic extrusion and deformation of western Indochina: structural and $^{40}Ar/^{39}Ar$ evidence from NW Thailand. J. Geophys. Res. 102 (B5), 10013–10037.

Lan, C.Y., Chen, C.H., Chung, S.L., Lee, T., Wang Lee, C.M., Yui, T.F., 1996. The crustal evolution of continental Taiwan. J. Geol. Soc. China 39, 337–353.

Lee, T.Y., Lawver, L.A., 1994. Cenozoic plate reconstruction of the South China Sea region. Tectonophysics 235, 149–180.

Lee, T.Y., Lawver, L.A., 1995. Cenozoic plate reconstruction of Southeast Asia. Tectonophysics 251, 85–138.

Leloup, P.H., Lacassin, R., Tapponnier, P., Schärer, U., Zhong, D.L., Liu, X.H., Zhang, L.S., Ji, S.C., Trinh, P.T., 1995. The Ailao Shan-Red River shear zone (Yunnan, China), tertiary transform boundary of Indochina. Tectonophysics 251, 3–84.

Li, S., Lin, C., Zhang, Q., Yang, S., Wu, P., 1998. The dynamic process of screen rift of continental marginal basin in northern South China Sea and the tectonic events since 10 Ma. Chin. Sci. Bull. 43 (8), 797–810.

Lin, A.T., Watts, A.B., Hesselbo, S.P., 2003. Cenozoic stratigraphy and subsidence history of the South China Sea margin in the Taiwan region. Basin Res. 15, 453–478.

Lin, G., Wang, Y.H., Guo, F., Wang, Y.J., Fan, W.M., 2004. Geodynamic modeling of crustal deformation of the North China Block: a preliminary study. J. Geophys. Eng. 1, 63–69.

Liu, H., Xia, B., Deng, W., Zhang, Y., 2004. Study of ^{40}Ar–^{39}Ar and K–Ar dating on the high-k volcanic rock from Bamaoqiongzong to Qiangbaqian in the Northern Tibet. J. Miner. Pertol. 24, 71–75.

Liu, H., Xia, B., Zhang, Y., 2003. The Shrimp U–Pb age of Matouwan diopside granite porphyry in Yunnan Province. Acta Geosci. Sin. 24, 552–554.
McKenzie, D., 1990. Spinning continents. Nature 344, 109–110.
Ord, A., 1991. Deformation of rock: a pressure-sensitive, dilatant material. Pure Appl. Geophys. 137, 337–366.
Ord, A., Oliver, N.H.S., 1997. Mechanical controls on fluid flow during regional metamorphism: some numerical models. J. Metamorphic Geol. 15, 345–359.
Pautot, G., Rangin, C., Briais, A., Tapponnier, P., Beuzart, P., Lericolais, G., Mathieu, X., Wu, J., Han, S., Li, H., Lu, Y., Zhao, J., 1986. Spreading direction in the central South China Sea. Nature 321, 150–154.
Ranalli, G., 1987. Rheology of the Earth. Allen and Unwin, London, p. 365.
Rangin, C., Klein, M., Roqoes, D., Le Pichon, X., Le Van, T., 1995. The Red River Fault system in the Tonkin Gulf, Vietnam. Tectonophysics 243, 209–222.
Reinecker, J., Heidback, O., Tingay, M., Connolly, P., Müller, B., 2004. The 2004 release of the world stress map (available online at www.world-stress-map.org).
Ren, J.S., Jin, X.C., 1996. New observations of the Red River Fault. Geol. Rev. 42 (5), 439–442.
Robert, H., 1997. Cenozoic plate tectonic reconstruction of SE Asia. In: Fraser, A.J., Matthews, S.J., Murphy, R.W. (Eds.), Petroleum Geology of Southeast Asia, vol. 126. Geological Society of London Special Publication, pp. 11–23.
Schärer, L., Zhang, P., Tapponnier, 1994. Ivanov–Smolensky conditioning: relationship between CR and UR form and intensity. Biol. Psychol. 37 (3), 247–258.
Shen, Z., Zhao, C., Yin, A., Li, Y., Jackson, D.D., Fang, P., Dong, D., 2000. Contemporary crustal deformation in east Asia constrained by Global Positioning System measurements. J. Geophys. Res. 105 (B3), 5721–5734.
Sorjonen-Ward, P., Zhang, Y., Zhao, C., 2002. Numerical modeling of orogenic processes and gold mineralization in the southeastern part of the Yilgarn Craton, Western Australia. Aust. J. Earth Sci. 49, 1011–1039.
Stern, R.J., Lin, P.N., Morris, J.D., 1990. Enriched back-arc basin basalts from the northern Marianna Trough: implications for the magmatic evolution of back-arc basin. Earth Planet Sci. Lett. 100, 210–225.
Strayer, L.M., Hudleston, P.J., Lorig, L.J., 2001. A numerical model of deformation and fluid-flow in an evolving thrust wedge. Tectonophysics 335, 121–145.
Sun, Z., Zhou, D., Zhong, Z., Zeng, Z., Wu, S., 2003. Experimental evidence for the dynamics of the formation of the Yinggehai basin, NW South China Sea. Tectonophysics 372, 41–58.
Tapponnier, P., Molnar, P., 1976. Slip-line field theory and large scale continental tectonics. Nature 264, 319–324.
Tapponnier, P., Peltzer, G., Armijo, R., 1986. On the mechanics of the collision between India and Asia. In: Coward, M.P., Ries, A.C. (Eds.), Collision Tectonics. Blackwell, Oxford, pp. 115–157.
Tapponnier, P., Peltzer, G., Le Dain, A.Y., Armijo, R., Cobbold, P., 1982. Propagating extrusion tectonics in Asia: new insights from simple experiments with plasticine. Geology 10, 611–616.
Tapponnier, P., Lacassin, R., Leloup, P.H., Scharer, U., Zhou, D., Wu, H., Liu, X., Ji, S., Zhang, L., Zhong, J., 1990. The Ailao-Shan/Red River metamorphic belt: tertiary left-lateral shear between Indochina and South China. Nature 343, 431–437.
Taylor, B., Hayes, D.E., 1980. The tectonic evolution of the South China Basin. In: Hayes, D.E. (Ed.), The Tectonic and Geologic Evolution of Southeast Asian Seas and Islands, Part 1. American Geophysical Union, vol. 23. Geophysical Monograph, Washington, DC, pp. 89–104.
Taylor, B., Hayes, D.E., 1983. Origin and history of the South China Sea Basin. In: Hayes, D.E. (Ed.), The Tectonic and Geologic Evolution of Southeast Asian Seas and Islands, Part 2. American Geophysical Union, vol. 27. Washington, DC, Geophysical Monograph, pp. 23–56.
Taylor, B., Rangin, C., 1988. Tertiary right-lateral pull-apart basins along the Asian-Pacific margin: constraints on the propagating extrusion model of Indo_Asian tectonics. In: Int. Symp. Geodynamic Evolution of Eastern Eurasian Margin, Paris, September 13–20, p. 100.
Treagus, S.H., 1973. Buckling stability of a viscous single-layer system, oblique to the principal compression. Tectonophysics 19, 271–289.
Tu, K., Xie, G., 1992. The geochemical characteristics of Cenozoic basalts from South China Sea and discussion for Duaple abnormal of isotope. In: Liu, R. (Ed.), The Ages and Geochemistry of Cenozoic Volcanic Rocks in China. Seismological Publishing House, Beijing, pp. 169–284.
Turcotte, D.L., Schubert, G., 1982. Geodynamics: Applications of Continuum Physics to Geological Problems. Wiley, New York, p. 450.
Vermeer, P.A., de Borst, R., 1984. Non-associated plasticity for soils, concrete and rock. Heron 29, 1–64.
Wang, C., Yang, J., Zhu, W., Zheng, M., 1995. Some problems in understanding basin evolution. Earth Sci. Frontiers 2, 29–44.
Wang, Y.J., Zhang, Y., Fan, W.M., Xi, X., Guo, F., Lin, G., 2002. Numerical modelling of the formation of Indo-Sinian peraluminous granitoids Hunan Province basaltic underplating versus tectonic thickening. Sci. China (D series) 45, 1042–1056.
Williams, J.R., Lewis, R.W., Zienkiewicz, O.C., 1978. A finite-element analysis of the role of initial perturbations in the folding of a single viscous layer. Tectonophysics 45, 187–200.
Wu, H.W., Zhang, L.S., Ji, S.C., 1989. The Red River-Ailaoshan Fault Zone—a Himalayan large sinistral strike-slip intercontinental shear zone. Sci. Geol. Sin. (1), 1–8.
Wu, J., 1988. Cenozoic basins in the South China Sea. Episodes 11, 91–95.
Xia, B., Cui, X.J., Xie, J.H., Wang, R., 2004. Thinking about the dynamics mechanism study on formation and evolution of South China Sea. Geotectonica Metall. 28, 221–227.
Xie, G., Tu, K., Wang, J., Zhang, M., Martin, F.J., Flower, 1989. The geographical distribution and genesis of Pb isotope components from Cenozoic basalts in Eastern China. Chin. Sci. Bull. 10, 772–775.
Xu, Y., Liu, J.H., Liu, F.T., Sun, H.B., He, T.Y., Jiang, W.W., 2003. The Ailao Shan-Red River Fault zone and crust-upper mantle structure of its adjacent regions. Sci. China (series D) 33 (12), 1201–1208.
Zhang, Y., Hobbs, B.E., Ord, A., Barnicoat, A., Zhao, C., Walshe, J.L., Ge, L., 2003. The influence of faulting on host-rock permeability, fluid flow and ore genesis of gold deposits: a theoretical 2D numerical model. J. Geochem. Exploration 78–79, 279–284.
Zhang, Y., Hobbs, B.E., Ord, A., Mühlhaus, H.-B., 1996a. Computer simulation of single layer buckling. J. Struct. Geol. 18, 643–655.

Zhang, Y., Mancktelow, Neil, S., Hobbs, B.E., Ord, A., Mühlhaus, H.-B., 2000. Numerical modelling of single-layer folding: clarification of an issue regarding the effect of computer codes and the influence of initial irregularities. J. Struct. Geol. 22, 1511–1522.

Zhang, Y., Scheibner, E., Hobbs, B.E., Ord, A., Drummond, B.J., Cox, S.J.D., 1998. Lithospheric structure in Southeast Australia: a model based on gravity, geoid and mechanical analyses. In: Braun, J., Dooley, J., Goleby, B., van der Hilst, R., Klootwijk, C. (Eds.), Structure and Evolution of the Australian Continent. AGU monograph, Geodynamics Series, vol. 26, pp. 89–108.

Zhang, Y., Scheibner, E., Ord, A., Hobbs, B.E., 1996b. Numerical modelling of crustal stresses in the eastern Australian passive margin. Aust. J. Earth Sci. 43, 161–175.

Zhang, P.Z., Wang, Q., Ma, Z.J., 2002. GPs velocity field and active crustal blocks of contemporary tectonic deformation in continental China. Earth Sci. Frontiers 9 (2), 430–441.

Zhang, L., Zhong, D., 1996. View on the Cenozoic tectonics of the Southeast Asia based on the strike-slip motion of the Red River shear zone. Sci. Geol. Sin. 31, 327–339.

Zhong, D.L., Tapponnier, P., Wu, H., Zhang, L., Ji, S., Zhong, J., Liu, X., Schärer, U., Lacassin, R., Leoup, P., 1989. Large-scale strike-slip faults—the important manner of post-collision intracontinental deformation. Chin. Sci. Bull. 7, 526–529.

Zhou, D., Ru, K., Chen, H.Z., 1995. Kinematics of Cenozoic extension on the South China Sea continental margin and its implications for the tectonic evolution of the region. Tectonophysics 251, 161–177.

Zhu, B., Wang, H., 1989. Nd–Sr–Pb isotope and chemical evidence for the volcanism with MORB-OIB source characteristics in the Leiqiong area, China. Geochimica 18 (3), 193–201.

Zhu, B., Wang, H., Chen, Y., Chang, X., Hu, Y.X.J., 2002. Geochronological and geochemical constraint on the Cenozoic extension of Cathaysian lithosphere and tectonic evolution of the border sea basins in East China. Geochimica 31 (3), 213–221.